



A numerical investigation of some RBF-FD error estimates

Elisabeth Larsson^a · Boštjan Mavrič^{a,b} · Andreas Michael^a · Fatemeh Pooladi^{a,c}

Abstract

In a recent paper by Tominec, Larsson and Heryudono a convergence proof for an oversampled version of the RBF-FD method, using polyharmonic spline basis functions augmented with polynomials, was derived. In this paper, we take a closer look at the individual estimates involved in this proof. We investigate how large the bounds are and how they depend on the node layout, the stencil size, and the polynomial degree. We find that a moderate amount of oversampling is sufficient for the method to be stable when Halton nodes are used for the stencil approximations, while a random node layout may require a very high oversampling factor. From a practical perspective, this indicates the importance of having a locally quasi uniform node layout for the method to be stable and give reliable results. We see an overall growth of the error constant with the polynomial degree and with the stencil size.

1 Introduction

In a finite difference method, an unknown function is represented as a (tensor product) polynomial interpolant of discrete function values on a grid. As an example, for $x_1 = -h$, $x_2 = 0$, $x_3 = h$, and corresponding function values $u(x_i) = u_i$ we have

$$u_h(x) = \frac{x(x-h)}{2h^2}u_1 - \frac{(x+h)(x-h)}{h^2}u_2 + \frac{(x+h)x}{2h^2}u_3 \equiv \sum_{i=1}^3 L_i(x)u_i. \quad (1)$$

If we differentiate the approximation and evaluate the result at $x = 0$, we get the well known results $u'_h(0) = \frac{u_3 - u_1}{2h}$ and $u''_h(0) = \frac{u_1 - 2u_2 + u_3}{h^2}$. However, we can also evaluate the function $u'_h(x) = \frac{2x-h}{2h^2}u_1 - \frac{2x}{h^2}u_2 + \frac{2x+h}{2h^2}u_3$ at any other point in the interval to get, e.g., $u'_h(\frac{h}{2}) = \frac{u_3 - u_2}{h}$. The Lagrange interpolation polynomial basis functions $L_j(x)$ used here are the cardinal basis functions of the finite difference stencil, meaning that $L_j(x_i) = \delta_{ij}$.

In the radial basis function-generated finite difference method (RBF-FD) [6] a similar approach is taken, but function values (nodal values) are instead given at scattered node locations and the underlying interpolation is multivariate and based on radial basis functions (RBF) instead of polynomials. We pay particular attention to RBF-FD methods where the interpolant consists of a combination of polyharmonic spline (PHS) basis functions $\phi(r) = r^{2i+1}$, $i \geq 0$, and polynomial basis functions of degree $\leq p$. This combination has been shown to perform well in a series of papers [5, 4, 3, 2]. The order of convergence is determined by the polynomial degree p , the approximations are comparatively well-behaved near boundaries, where stencils become skewed, and there is no need to tune a shape parameter as for some other choices of RBFs.

In RBF-FD, for a point $x_k \in X \subset \mathbb{R}^d$, where $X = \{x_k\}_{k=1}^N$ is a global scattered node set, we form a stencil based on the set $X_k = \{x_j^{(k)}\}_{j=1}^n$ of the $n \ll N$ nearest neighbors of x_k , and we let $x_1^{(k)} = x_k$. We form a local interpolant $u_h(x)$ using $\phi(r) = r^3$ and monomials p_j that form a basis for polynomials of degree p , such that

$$u_h(x) = \sum_{j=1}^n \lambda_j^{(k)} \phi(\|x - x_j^{(k)}\|_2) + \sum_{j=1}^m \mu_j^{(k)} p_j(x), \quad (2)$$

under the constraint $\sum_{j=1}^n \lambda_j^{(k)} p_\ell(x_j^{(k)}) = 0$, $\ell = 1, \dots, m$. This interpolant is not on cardinal form, i.e., the unknown coefficients are not the nodal values. To transfer it to cardinal form, we use (2) for each stencil point, which results in the linear system

$$\begin{pmatrix} A^{(k)} & P^{(k)} \\ (P^{(k)})^T & \mathbf{0} \end{pmatrix} \begin{pmatrix} \underline{\lambda}^{(k)} \\ \underline{\mu}^{(k)} \end{pmatrix} = \begin{pmatrix} u(X_k) \\ \underline{0} \end{pmatrix} \Rightarrow \begin{pmatrix} \underline{\lambda}^{(k)} \\ \underline{\mu}^{(k)} \end{pmatrix} = \begin{pmatrix} A^{(k)} & P^{(k)} \\ (P^{(k)})^T & \mathbf{0} \end{pmatrix}^{-1} \begin{pmatrix} u(X_k) \\ \underline{0} \end{pmatrix}, \quad (3)$$

where $A^{(k)}$ has elements $a_{ij} = \phi(\|x_i^{(k)} - x_j^{(k)}\|_2)$ and $P^{(k)}$ has elements $p_{ij} = p_j(x_i^{(k)})$. The vectors $\underline{\lambda}^{(k)} = (\lambda_1^{(k)}, \dots, \lambda_n^{(k)})^T$, $\underline{\mu}^{(k)} = (\mu_1^{(k)}, \dots, \mu_m^{(k)})^T$, and $u(X_k) = (u(x_1^{(k)}), \dots, u(x_n^{(k)}))^T$. The system matrix is non-singular if the node points are distinct, and P has full rank. The latter puts some restrictions on the node layout. For example, Cartesian node layouts can lead to rank deficiency in skewed stencils near the boundaries if the stencil size is too small. A method to overcome problems of rank deficiency in the polynomial part of an RBF-FD approximation can be found in [7], but here, we restrict our investigations to node layouts that are unisolvent for polynomials of degree p .

The authors are listed in alphabetical order.

^aScientific Computing, Dept. of Information Technology, Uppsala University, Uppsala, Sweden.

^bFaculty of Mechanical Engineering, University of Ljubljana, Ljubljana, Slovenia.

^cDept. of Mathematics, Persian Gulf University, Bushehr, Iran.

In the same way as in the finite difference case, we can now evaluate the local interpolant or its derivatives at any point y . We have

$$\begin{aligned}
 u_h(y) &= \sum_{j=1}^n \lambda_j \phi(\|y - x_j^{(k)}\|_2) + \sum_{j=1}^m \mu_j p_j(y) \\
 &= \left(\phi(\|y - x_1^{(k)}\|_2) \cdots \phi(\|y - x_n^{(k)}\|_2) \ p_1(y) \cdots p_m(y) \right) \begin{pmatrix} \lambda^{(k)} \\ \mu^{(k)} \end{pmatrix} \\
 &= \left(\phi(\|y - x_1^{(k)}\|_2) \cdots \phi(\|y - x_n^{(k)}\|_2) \ p_1(y) \cdots p_m(y) \right) \begin{pmatrix} A^{(k)} & P^{(k)} \\ (P^{(k)})^T & \mathbf{0} \end{pmatrix}^{-1} \begin{pmatrix} u(X_k) \\ \mathbf{0} \end{pmatrix} \\
 &\equiv \left(\psi_1^{(k)}(y) \cdots \psi_n^{(k)}(y) \ \eta_1^{(k)}(y) \cdots \eta_m^{(k)}(y) \right) \begin{pmatrix} u(X_k) \\ \mathbf{0} \end{pmatrix}. \tag{4}
 \end{aligned}$$

That is, we can express the local interpolant on cardinal form as

$$u_h(y) = \sum_{j=1}^n u(x_j^{(k)}) \psi_j^{(k)}(y), \tag{5}$$

and the cardinal functions (weights) are computed from the vector of PHS and polynomial basis functions and the inverse of the local interpolation matrix as shown in (4). Weights for differentiation are found by differentiating the cardinal basis functions. If we apply a linear differential operator to the local interpolant we get

$$\mathcal{L}u_h(y) = \sum_{j=1}^n u(x_j^{(k)}) \mathcal{L}\psi_j^{(k)}(y). \tag{6}$$

In [10], we used the capability of the method to evaluate the approximation anywhere to construct a least-squares or oversampled RBF-FD method. For each evaluation point y , in our method, we choose the stencil with its center x_k closest to y for evaluation. This corresponds to an implicit Voronoi decomposition of the computational domain (see Figure 1), and it results in the global solution/interpolant having a (small) jump across each Voronoi region edge, where we switch stencils. For further discussion of the global discontinuous trial space V_h , see [10]. A small stencil with seven evaluation points in the corresponding Voronoi region is shown in the left part of Figure 1.

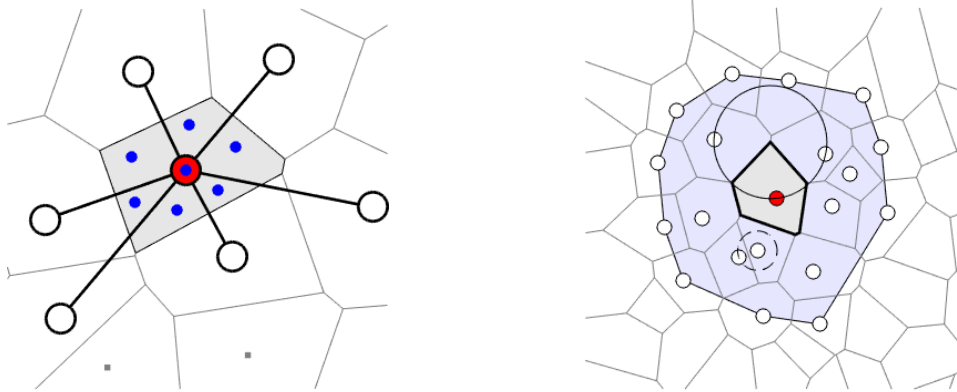


Figure 1: Left: A scattered node stencil, the Voronoi region belonging to the center point, and seven evaluation points (small, blue) in the Voronoi region. Right: A Voronoi tessellation over Halton nodes, a stencil with $n = 20$ node points (round markers), the convex hull of the node points (shaded), the Voronoi region (thick black line) of the center point (red), the circles defining the fill distance (solid circle), and the doubled separation distance (dashed circle).

In [10], we also analyzed the convergence properties of the oversampled RBF-FD method for a Poisson problem with mixed boundary conditions.

$$\begin{cases} \Delta u = f_2, & \text{in } \Omega, \\ \nabla u \cdot \hat{n} = f_1, & \text{on } \partial\Omega_1, \\ u = f_0, & \text{on } \partial\Omega_0, \end{cases} \tag{7}$$

where \hat{n} is the outward unit normal and $\partial\Omega = \partial\Omega_0 \cup \partial\Omega_1$. We used estimates involving norms over the Voronoi regions \mathcal{V}_k where, due to the cubic PHS basis, the local interpolants $u_h|_{\mathcal{V}_k} \in C^2$. As an introduction to the estimates, we first introduce the L_2 -norm over one Voronoi region \mathcal{V}_k , associated with one nodal point x_k

$$\|u_h\|_{L_2(\mathcal{V}_k)}^2 = \int_{\mathcal{V}_k} u_h(y)^2 dy = u_h(X_k)^T M u_h(X_k), \tag{8}$$

where the elements of the local mass matrix M are given by $m_{ij} = \int_{\mathcal{V}_k} \psi_i^{(k)}(y) \psi_j^{(k)}(y) dy$. When several local matrices are involved, we also use the notation $M^k = M$. We note that the eigenvalues of the mass matrix provide an upper bound for the norm in relation to the discrete values

$$\|u_h\|_{L_2(\mathcal{V}_k)}^2 \leq \max_i \alpha_i \|u_h(X_k)\|_2^2, \quad (9)$$

where $\alpha_i > 0$ are the eigenvalues of the mass matrix. We also introduce the discrete counterpart, where we define the norm as

$$\|u_h\|_{\ell_2(\mathcal{V}_k)}^2 = \frac{|\mathcal{V}_k|}{|Y_k|} u_h(Y_k)^T u_h(Y_k) = u_h(X_k)^T E_h^T E_h u_h(X_k) = u_h(X_k)^T M u_h(X_k), \quad (10)$$

where $Y_k \in \mathcal{V}_k$ are the evaluation points associated with stencil k , where the elements of the local evaluation matrix E_h are given by $e_{qi} = \sqrt{\frac{|\mathcal{V}_k|}{|Y_k|}} \psi_i^{(k)}(y_q)$, and where the elements of the discrete mass matrix are given by $m_{ij} = \frac{|\mathcal{V}_k|}{|Y_k|} \sum_{y_q \in Y_k} \psi_i^{(k)}(y_q) \psi_j^{(k)}(y_q)$. We note that the discrete norm can be interpreted as an approximation of the continuous norm, where a discrete quadrature has been introduced. We get the corresponding global discrete norm by summing over all Voronoi regions such that

$$\|u_h\|_{\ell_2(\Omega)}^2 = \sum_{k=1}^N \|u_h\|_{\ell_2(\mathcal{V}_k)}^2. \quad (11)$$

When solving the PDE (7), we introduce three different global point sets Y^i , $i = 0, 1, 2$, to discretize the three equations on their respective domains. The discrete norms on the boundary are, similarly to (10) and (11), given by

$$\|u_h\|_{\ell_2(\partial\Omega_i)}^2 = \sum_{k=1}^N \|u_h\|_{\ell_2(\mathcal{V}_k \cap \partial\Omega_i)}^2 = \frac{|\mathcal{V}_k \cap \partial\Omega_i|}{|Y_k^i|} u_h(Y_k^i)^T u_h(Y_k^i). \quad (12)$$

The total number of unknowns in the PDE discretization is equal to the number of node points $|X| = N$ and the unknowns are the nodal values $u_h(X)$. If $|Y| = |Y^0| + |Y^1| + |Y^2| = N_y > N$, then the discrete system of equations is overdetermined and we solve the problem in the least squares sense. That is, we minimize the square residual of the PDE problem, which is given by

$$\|r_h\|_{\ell_2(\Omega)}^2 = \beta_2^2 \|\Delta(u_h - u)\|_{\ell_2(\Omega)}^2 + \beta_1^2 \|\nabla(u_h - u) \cdot \hat{n}\|_{\ell_2(\partial\Omega_1)}^2 + \beta_0^2 \|u_h - u\|_{\ell_2(\partial\Omega_0)}^2, \quad (13)$$

where β_i represent the scaling of the different equations in the residual minimization. We choose the scaling to balance the three contributions across a Voronoi region during refinement, taking both the derivatives and the size of the local domain into account, which up to a constant factor leads to $\beta_2^2 = 1$, $\beta_1^2 = h^{-1}$, and $\beta_0^2 = h^{-3}$ in two spatial dimensions, where h is the fill distance of the node set X , see Section 2 for a definition. We can rewrite the minimization problem in terms of a bilinear and a linear form in the following way:

$$\text{Find } u_h \in V_h \text{ such that } a_h(u_h, v_h) = \ell_h(f, v_h), \quad \forall v_h \in V_h, \quad (14)$$

where

$$a_h(u_h, v_h) = \beta_2^2 (\Delta u_h, \Delta v_h)_{\ell_2(\Omega)} + \beta_1^2 (\nabla u_h \cdot \hat{n}, \nabla v_h \cdot \hat{n})_{\ell_2(\partial\Omega_1)} + \beta_0^2 (u_h, v_h)_{\ell_2(\partial\Omega_0)}, \quad (15)$$

$$\ell_h(f, v_h) = \beta_2^2 (f_2, \Delta v_h)_{\ell_2(\Omega)} + \beta_1^2 (f_1, \nabla v_h \cdot \hat{n})_{\ell_2(\partial\Omega_1)} + \beta_0^2 (f_0, v_h)_{\ell_2(\partial\Omega_0)}. \quad (16)$$

Just as for a finite element method, we want to show coercivity of the bilinear form, because this guarantees that the discrete problem has a unique solution and that the approximation is stable, which is needed together with consistency for convergence. In [10], it was shown that this can be done with the help of an auxiliary function $v = S(v_h) \in W_2^2(\Omega)$, where $S(\cdot)$ is a smoothing operator, further described in Section 3 and $W_2^2(\cdot)$ is a Sobolev space. We introduce a continuous bilinear form $a(\cdot, \cdot)$ similar to (15), but with the ℓ_2 inner product replaced by the L_2 inner product, for functions in $W_2^2(\Omega)$. We also need a semi discrete norm

$$\|u_h\|_{L_2^*(\Omega)}^2 = \sum_{k=1}^N \|u_h\|_{L_2(\mathcal{V}_k)}^2, \quad (17)$$

which ignores any discontinuities between Voronoi regions. We associate a semi-discrete bilinear form $a^*(\cdot, \cdot)$ for functions in V_h with the L_2^* inner product.

The coercivity is shown in a series of steps, which include integration errors, τ_0 and τ_a when we pass between the discrete and semi discrete norms, and smoothing errors η_0 and η_a when we pass between the discontinuous trial space and the smoothed function space. Together with coercivity for the continuous PDE problem $\|v\|_{L_2(\Omega)} \leq C^2 a(v, v)$ these estimates yield

$$\begin{aligned} \|v_h\|_{\ell_2(\Omega)}^2 &\leq (1 + \tau_0) \|v_h\|_{L_2^*(\Omega)}^2 \\ &\leq (1 + \tau_0)(1 + \eta_0) \|v\|_{L_2(\Omega)}^2 \\ &\leq (1 + \tau_0)(1 + \eta_0) C^2 a(v, v) \\ &\leq (1 + \tau_0)(1 + \eta_0) C^2 (1 + \eta_a) a^*(v_h, v_h) \\ &\leq \frac{(1 + \tau_0)(1 + \eta_0) C^2 (1 + \eta_a)}{1 - \tau_a} a_h(v_h, v_h). \end{aligned}$$

Combined with an estimate for the interpolation error [2, 10], the coercivity provides the final error estimate

$$\|u_h - u\|_{\ell_2(\Omega)} \leq \sqrt{2}C \left(\frac{(1 + \tau_0)(1 + \eta_0)(1 + \eta_a)}{(1 - \tau_a)} \right)^{\frac{1}{2}} (c_0 h^{p+1} + c_1 h^p + c_2 h^{p-1}) |u|_{W_\infty^{p+1}(\Omega)}, \quad (18)$$

assuming that u has sufficient smoothness.

In this paper we look more carefully into the error constants that affect the approximation stability of the method, to see how they depend on properties of the node layout and the basis functions. Section 2 introduces some general concepts. In Sections 3 and 4, we discuss the theoretical properties of the smoothing errors and the integration errors. Sections 5 and 6 contain numerical results for the two types of errors, and we finish the paper with a discussion of the results in Section 7.

2 General stencil, node, and approximation properties

The local fill distance h is the radius of the largest ball empty of nodes within the stencil

$$h = \sup_{x \in \Omega_k} \min_{x_j \in X_k} \|x - x_j\|_2, \quad (19)$$

where Ω_k , e.g., can be chosen as the convex hull of the stencil nodes as in the right part of Figure 1. We define the local separation distance s as half of the smallest distance between two points in the stencil

$$s = \frac{1}{2} \min_{\substack{j \neq k \\ x_j, x_k \in X_k}} \|x_j - x_k\|_2. \quad (20)$$

We measure node quality as $c_q = s/h < 1$, which is largest for a quasi uniform node layout and small for a random node distribution.

When we compare results for different stencils, we scale the nodes such that $h = 1$, which corresponds to a transformation $\tilde{x} = x/h$. This means that if we compute derivatives (or integrals) for $h \neq 1$, the fill distance appears as a metric coefficient that needs to be taken into account. That is, $\frac{\partial^\alpha}{\partial x^\alpha} = h^{|\alpha|} \frac{\partial^\alpha}{\partial \tilde{x}^\alpha}$ and $dx = h^d d\tilde{x}$ for a differential element in d dimensions.

When we investigate local estimates of derivatives, the polynomial part of the trial space has a null space. This null space is in general not harmful to the estimates as polynomial data up to degree p is represented exactly, but the null space needs to be removed from the generalized eigenproblems that we study in order to have reliable computations. We use the following general strategy for null space removal in the case where B has a nullspace in the generalized eigenproblem $Av = \lambda Bv$ of size n :

1. Perform the singular value decomposition $B = USV^T$.
2. Let $r < n$ be the rank of B and write the decomposition on block form such that $U = (U_r \ U_0)$, $S = \begin{pmatrix} S_r & 0 \\ 0 & 0 \end{pmatrix}$, and $V = (V_r \ V_0)$.
We note that $B = USV^T = U_r S_r V_r^T$.
3. We write the eigenvectors as $v = V_r V_r^T v + V_0 V_0^T v$ and multiply the eigenproblem from the left by U_r^T to get $U_r^T A V_r V_r^T v + U_r^T A V_0 V_0^T v = \lambda S_r V_r^T v + 0 V_0^T v$.
4. We let $C = U_r^T A V_r$ and note that the relevant eigenvalues correspond to the transformed generalized eigenproblem $C V_r^T v = \lambda S_r V_r^T v$.
5. We recover the original eigenvectors from $y = V_r^T v$ as $v = V_r y$.

Note that we can find the dimensions of the polynomial null spaces analytically, such that we do not need to rely on a numerical estimate of the rank. Throughout the paper, all numerical experiments are performed using MATLAB. The generalized eigenvalue problem is computed with `eig`, which uses Cholesky factorization for a symmetric A and symmetric positive definite B , and the QZ algorithm for general matrices.

3 The smoothing error estimates

The smoothing error measures the distance between the discontinuous trial space and the Sobolev space $W_2^2(\Omega)$, for the norm and for the bilinear form. In order to derive these estimates, in [10], we (theoretically) formed a smoothing operator based on partition of unity blending of the local stencil approximations evaluated on overlapping extended Voronoi regions, which we denote by V_k^δ . The smoothed function has the form

$$v = S(v_h) = \sum_{j=1}^N \omega_j(y) v_h^j(y) = \sum_{j \in J_k} \omega_j(y) v_h^j(y), \quad y \in \mathcal{V}_k,$$

where $\omega_j(y)$ are partition of unity weight functions supported on V_j^δ and J_k contains the indices of the extended Voronoi regions that overlap with \mathcal{V}_k . We also define $\tilde{J}_k = J_k \setminus k$ for later use.

An illustration of how this smoothing works in one dimension is shown in Figure 2. For each Voronoi region \mathcal{V}_k the trial space functions have the property $v_h \in C^2(\mathcal{V}_k)$. That is, the Laplacian shown in the left part of the figure is continuous within each region (same color), but is slightly different at each Voronoi interface (color change). A close-up of the overlap region around the interface is shown in the right part of the figure. To connect the functions coming from the left and right sides such that the overall result is C^2 , the blended function needs to make a wiggle.

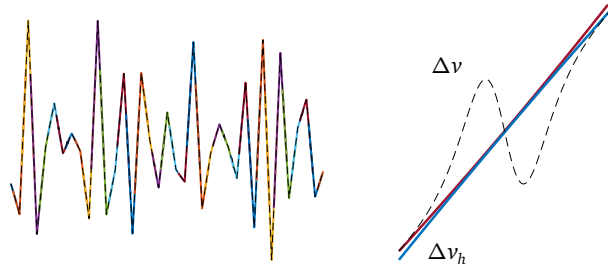


Figure 2: To the left, the Laplacian of a one-dimensional trial space function with random nodal data is shown. To the right, a region with two overlapping stencil functions (solid lines) is shown. The function v is a C^2 blending of the two and its Laplacian (dashed line) performs a wiggle that compensates for the local discontinuity.

To make the realizations of the smoothing error bounds computable, we need to go a little bit further with the actual construction of the extended Voronoi regions than we did in [10]. To make an extension of relative size δ of the Voronoi region belonging to the point x_k , for each vertex v_i , we compute the extended vertex $v_i^\delta = (1 + \delta)v_i - \delta x_k$. The right part of Figure 3 provides a visualization of the extended Voronoi regions. Note that the width of the overlap between two Voronoi regions varies with the distance between the respective points associated with the regions. We let \mathcal{V}_k^δ denote the extended Voronoi region, we let $\Gamma_{k,j}^\delta = \mathcal{V}_k \cap \mathcal{V}_j^\delta$ (illustrated with colored point markers in Figure 3), we let $\mathcal{V}_k^{-\delta} = \mathcal{V}_k \setminus \left(\bigcup_{j \in \bar{J}_k} \Gamma_{k,j}^\delta \right)$ denote the non-overlapped part of the Voronoi region, and we let $\Gamma_k^\delta = \mathcal{V}_k \setminus \mathcal{V}_k^{-\delta}$.

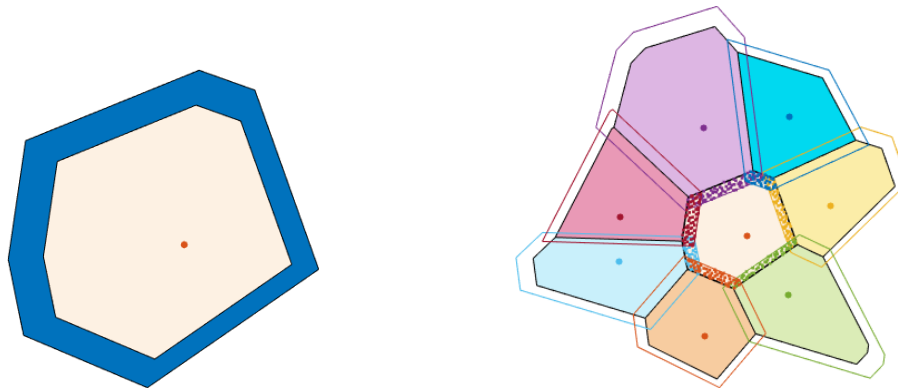


Figure 3: Left: A Voronoi region divided into the non-overlapped part $\mathcal{V}_k^{-\delta}$ and the band Γ_k^δ for $\delta = 0.2$. Right: The same Voronoi region and its neighbors are shown with different fill colors. The intersections between the extended neighbor regions (colored lines) and the central region are shown with colored point markers. Note that the different intersections overlap where they meet.

We have not actually constructed the weight functions for the Voronoi regions, but we suggest the following steps as a potential approach. First, we define appropriate barycentric coordinates $z_1(y), \dots, z_{n_v}(y)$, $0 \leq z_i \leq 1$, in \mathcal{V}_k , where n_v is the number of vertices of the region. A method to construct non-negative barycentric coordinates with sufficient continuity is provided in [1]. Then we can construct a non-negative tensor product generating function over the region as $\varphi_k(y) = \varphi_0(z_1) \cdots \varphi_0(z_{n_v})$, where $\varphi_0(x)$ is positive on $(0, 1)$ and $\varphi_0(0) = \varphi_0(1) = 0$. Finally, we use Shepard’s method [8] to compute the weight functions as

$$\omega_k(y) = \frac{\varphi_k(y)}{\sum_{j \in \bar{J}_k} \varphi_j(y)}. \tag{21}$$

We need to estimate the derivatives of the weight functions that go into the smoothing estimates. In the numerical experiments, we do this by computing a one-dimensional weight function with the correct node distance and overlap and its derivatives. Here we note that for an overlap region of width δh and a generating function that depends polynomially on the argument, a derivative of order k across the overlap is proportional to $(\delta h)^{-k}$. That is, a small overlap gives very large derivatives. In our way of constructing the overlap regions, this happens when two node points x_j and x_k are close to each other. That is, when the separation distance s , and hence the node quality c_q , is small.

The smoothing error estimates in [10, Theorem 4.3] that we want to investigate are $\|v_h\|_{L_2(\Omega)}^2 \leq (1 + \eta_0)\|v\|_{L_2(\Omega)}^2$, and $a(v, v) \leq (1 + \eta_a)a^*(v_h, v_h)$. The global error constants η_0 and η_a are derived based on local estimates over each Voronoi region. For the first estimate we need the local bound $\eta_{k,0}$ given by

$$\frac{\|v_h\|_{L_2(\mathcal{V}_k)}^2}{\|v\|_{L_2(\mathcal{V}_k)}^2} = \frac{\|v_h\|_{L_2(\mathcal{V}_k^{-\delta})}^2 + \|v_h\|_{L_2(\Gamma_k^\delta)}^2}{\|v_h\|_{L_2(\mathcal{V}_k^{-\delta})}^2 + \|v\|_{L_2(\Gamma_k^\delta)}^2} \leq 1 + \frac{\|v_h\|_{L_2(\Gamma_k^\delta)}^2}{\|v_h\|_{L_2(\mathcal{V}_k^{-\delta})}^2} = 1 + \frac{v_h(X_k)^T M_{\Gamma_k^\delta} v_h(X_k)}{v_h(X_k)^T M_{\mathcal{V}_k^{-\delta}} v_h(X_k)} \leq 1 + \eta_{k,0}, \tag{22}$$

where $\eta_{k,0}$ is the largest eigenvalue of the generalized eigenproblem $M_{\Gamma_k^\delta} v_h = \eta M_{\mathcal{V}_k^{-\delta}} v_h$, and where $M_{\mathcal{D}}$ denotes the continuous norm mass matrix with integration restricted to the domain \mathcal{D} . The global constant is the maximum over the Voronoi regions of the local constant. The bound is expected to be pessimistic due to the following reasons:

- We replace the smoothed function v in the overlap region by 0 in the denominator. However, since the neighboring stencils share a significant part of their data, we expect v and v_h to be similar in the overlap region. The size of the jumps in the global cardinal functions between Voronoi regions was investigated in [9], and shown to be small, especially for large stencils.
- The global bound uses the worst case estimate for every stencil, but since the stencils share nodal values it is not realistic that the worst case scenario occurs in every Voronoi region simultaneously. The actual global smoothing error should therefore be smaller.

For the second smoothing error estimate, we first expand the bilinear form applied to the smoothed function on one Voronoi region

$$\begin{aligned} a(v, v)_{\mathcal{V}_k} &= a(v, v)_{\mathcal{V}_k^{-\delta}} + a(v, v)_{\Gamma_k^\delta} = a(v_h^k, v_h^k)_{\mathcal{V}_k^{-\delta}} + \sum_{i \in J_k} \sum_{j \in J_k} a(\omega_i v_h^i, \omega_j v_h^j)_{\Gamma_k^\delta \cap \mathcal{V}_i^\delta \cap \mathcal{V}_j^\delta} \\ &\leq a(v_h^k, v_h^k)_{\mathcal{V}_k} + Q \sum_{j \in J_k} a(\omega_j v_h^j, \omega_j v_h^j)_{\Gamma_k^\delta \cap \mathcal{V}_j^\delta}, \end{aligned} \quad (23)$$

where Q is the maximum number of extended Voronoi regions that overlap at any one point. To get the global estimate, we again first study local bounds for the sum. This estimate is more involved due to the fact that the Laplacian operator (as well as the gradient operator) has a polynomial nullspace, and the bilinear form involving the smoothed function may be non-zero in $\Gamma_{k,j}^\delta$ even if the bilinear form applied to the trial space function is zero in \mathcal{V}_k [10]. To make sure that the numerator and denominator are either both zero or both non-zero, the estimate involves all the Voronoi regions in J_k . We are not going to make a full study of the local estimates for the bilinear form. Instead, for simplicity, we focus on the main case of a Voronoi region and its neighboring regions located in the interior of the domain such that the bilinear form does not include the boundary terms. With this restriction, the local estimates to investigate become

$$\begin{aligned} \frac{\sum_{j \in J_k} a(\omega_j v_h^j, \omega_j v_h^j)_{\Gamma_{k,j}^\delta}}{\sum_{j \in J_k} a(v_h^j, v_h^j)_{\mathcal{V}_j}} &\leq \frac{\sum_{j \in J_k} \|\Delta(\omega_j v_h^j)\|_{L_2(\Gamma_{k,j}^\delta)}^2}{\sum_{j \in J_k} \|\Delta v_h^j\|_{L_2(\mathcal{V}_j)}^2} \\ &\leq \frac{2 \sum_{j \in J_k} \|\omega_j\|_{L_2(\Gamma_{k,j}^\delta)}^2 \|\Delta v_h^j\|_{L_2(\Gamma_{k,j}^\delta)}^2 + 2 \|\nabla \omega_j\|_{L_2(\Gamma_{k,j}^\delta)}^2 \|\nabla v_h^j\|_{L_2(\Gamma_{k,j}^\delta)}^2 + \|\Delta \omega_j\|_{L_2(\Gamma_{k,j}^\delta)}^2 \|v_h^j\|_{L_2(\Gamma_{k,j}^\delta)}^2}{\sum_{j \in J_k} \|\Delta v_h^j\|_{L_2(\mathcal{V}_j)}^2} \\ &= \frac{2 \sum_{j \in J_k} v_h(X_j)^T \left(\|\omega_j\|_{L_2(\Gamma_{k,j}^\delta)}^2 L_{\Gamma_{k,j}^\delta}^j + 2 \|\nabla \omega_j\|_{L_2(\Gamma_{k,j}^\delta)}^2 K_{\Gamma_{k,j}^\delta}^j + \|\Delta \omega_j\|_{L_2(\Gamma_{k,j}^\delta)}^2 M_{\Gamma_{k,j}^\delta}^j \right) v_h(X_j)}{\sum_{j \in J_k} v_h(X_j)^T L_{\mathcal{V}_j}^j v_h(X_j)}, \end{aligned} \quad (24)$$

where $L_{\mathcal{D}}^j$ is the matrix corresponding to the squared continuous norm of the Laplacian based on the stencil centered in x_j with nodes X_j , $K_{\mathcal{D}}^j$ is the corresponding matrix for the squared gradient, and $M_{\mathcal{D}}^j$ is the mass matrix associated with stencil j . We can again use a generalized eigenvalue problem to bound the local estimate, but we need to i) assemble the matrices associated with different stencils into larger matrices, and ii) remove the nullspace of the denominator, see Section 2. The vectors in the nullspace are harmless for the global estimate as in this case, the trial space function and the smoothed function are locally equal. The local upper bound $\eta_{k,a}$ is the largest eigenvalue of the generalized eigenvalue problem with an eigenvector not in the null space. The global constant is given by $\eta_a = 2Q \max_k \eta_{k,a} |J_k|$. This bound is also pessimistic, since we have made several worst case estimates and the bound is based on a worst case behaviour in each stencil.

4 The integration error estimates

The integration error estimate for the norm $\|v_h\|_{L_2(\Omega)}^2 \leq (1 + \tau_0) \|v_h\|_{L_2^s(\Omega)}^2$ relates the discrete and continuous norms. We note that the bound breaks down when $\tau_0 = -1$, which corresponds to the case of the discrete norm being zero for a non-zero function. It was shown in [10] that this cannot happen in the global problem if $X \subset Y$. Then any non-zero data will be sampled at least once by the discrete norm. Our task is therefore to investigate the upper bound for τ_0 .

In [10], a Monte Carlo integration bound was used in the theoretical discussion of the integration error. For a quasi uniform node set Y this leads to convergence approximately proportional to $1/N_y$. However, the Koksma-Hlawka variation that is included in the bound is difficult to estimate or compute, especially when the integration domain is not the unit square. In the paper, the total variation was mistakenly used, but this cannot be used to replace the Koksma-Hlawka variation. Then in [11], a simplified integration error estimate for evaluation points on a grid was derived. Here, we extend the simplified bound to quasi uniform evaluation points. We make the following assumption: The Voronoi region \mathcal{V}_k contains q_k evaluation points $\{y_i^{(k)}\}_{i=1}^{q_k} = Y_k$ and can be divided into q_k smaller regions $\mathcal{V}_{k,i}$ of (equal) size $|\mathcal{V}_k|/q_k$, such that $y_i^{(k)} \in \mathcal{V}_{k,i}$. We include the size of the local region in

the quadrature formula, which is possible, but not necessary for the oversampled RBF-FD method. We divide both the continuous global integral I and discrete global integral I_h into a sum of integrals over these smaller regions such that

$$I = \int_{\Omega} v_h(y) dy = \sum_{k=1}^N \int_{\mathcal{V}_k} v_h(y) dy = \sum_{k=1}^N \sum_{i=1}^{q_k} \int_{\mathcal{V}_{k,i}} v_h(y) dy, \quad (25)$$

$$I_h = \sum_{k=1}^N \frac{|\mathcal{V}_k|}{q_k} \sum_{i=1}^{q_k} v_h(y_i^{(k)}) = \sum_{k=1}^N \sum_{i=1}^{q_k} \int_{\mathcal{V}_{k,i}} v_h(y_i^{(k)}) dy. \quad (26)$$

To bound the integration error, we first make an upper bound for the difference of the integrands over a small region, using that $v_h \in C^2$ and letting h_y denote the fill distance of the evaluation point set Y ,

$$\max_{y \in \mathcal{V}_{k,i}} |v_h(y) - v_h(y_i^{(k)})| \leq \max_{y \in \mathcal{V}_{k,i}} |y - y_i^{(k)}| \max_{y \in \mathcal{V}_{k,i}} |\nabla v_h(y)| \leq c_{k,i} h_y \max_{y \in \mathcal{V}_k} |\nabla v_h(y)|, \quad (27)$$

where $c_{k,i}$ measures the variation in the largest distance inside the small regions. If we use this estimate for the global integration error we get

$$|I - I_h| \leq \sum_{k=1}^N \sum_{i=1}^{q_k} \frac{|\mathcal{V}_k|}{q_k} c_{k,i} h_y \max_{y \in \mathcal{V}_k} |\nabla v_h(y)| = h_y |\Omega| \frac{1}{N} \sum_{k=1}^N c_k \max_{y \in \mathcal{V}_k} |\nabla v_h(y)| \frac{1}{q_k} \sum_{i=1}^{q_k} c_{k,i}, \quad (28)$$

where c_k measures that variation in the size of the Voronoi regions. We note that the variation in size and shape of the Voronoi regions and their subdivisions contributes to increase the error constant. This bound implies linear convergence in h_y of the integration error, which is proportional to $1/\sqrt{N_y}$ in two dimensions. In our preliminary numerical experiments for the integration error, we computed the worst case estimate for the gradient over a Voronoi region. However, this resulted in very large bounds, suggesting that h_y would need to be very small and consequently, the oversampling would need to be very large.

Instead, when we investigate the bound numerically, we first consider the local error in one Voronoi region explicitly and write it on the form

$$\frac{\|v_h\|_{\ell_2(\mathcal{V}_k)}^2 - \|v_h\|_{L_2(\mathcal{V}_k)}^2}{\|v_h\|_{L_2(\mathcal{V}_k)}^2} = \frac{v_h(X_k)^T (M_h - M) v_h(X_k)}{v_h(X_k)^T M v_h(X_k)} \leq \tau_{k,0}, \quad (29)$$

where $\tau_{k,0}$ is the largest positive generalized eigenvalue. The global constant τ_0 is found as the maximum of the local constants. When we make this estimate over one Voronoi region, we need M_h to be full rank for all functions to be integrable. That is, we need to look at the subproblem as a global overdetermined problem. The oversampling factor in this case becomes q_k/n , indicating that we need $q_k \geq n$. For a global problem, we can typically use a q_k that is much smaller than n . The reason is that stencils overlap and share unknowns. For the global problem to be overdetermined we only need $q_k > 1$.

The difference between the global problem and the one Voronoi region problem is that in the first case, all nodes are inside some Voronoi region over which we integrate, due to skewed stencils at the boundary, while in the second case, only one node is inside the single Voronoi region and the other nodes are outside. This also means that q_k and h_y have slightly different relations. To make a generalizable estimate in between the two extremes, we choose to assemble the generalized eigenproblem for the Voronoi regions belonging to all points in a stencil. We let \mathcal{I}_k be the set of indices of the points in the stencil associated with x_k and compute

$$\frac{\sum_{j \in \mathcal{I}_k} (\|v_h\|_{\ell_2(\mathcal{V}_j)}^2 - \|v_h\|_{L_2(\mathcal{V}_j)}^2)}{\sum_{j \in \mathcal{I}_k} \|v_h\|_{L_2(\mathcal{V}_j)}^2} = \frac{\sum_{j \in \mathcal{I}_k} v_h(X_j)^T (M^j - M^j) v_h(X_j)}{\sum_{j \in \mathcal{I}_k} v_h(X_j)^T M^j v_h(X_j)} \leq \tilde{\tau}_{k,0}. \quad (30)$$

This system includes the nodes X_k of the central stencil as well as the nodes of the stencils centered at all the nodes in X_k . This means that the combined node layout extends around half a stencil outside of the central stencil. If a stencil of size n is approximately round, then the radius of the stencil $r_s \approx \sqrt{\frac{n}{\pi}}$ and the circumference $o_s \approx 2\pi r_s$. This means that the size of the extended system is approximately $n + r_s o_s = 3n$ and the oversampling factor becomes $q_k n / 3n$, leading to the requirement $q_k \gtrsim 3$, since there are n Voronoi regions with q_k points each.

For the bilinear form, the error estimate we need is $a^*(v_h, v_h) \leq \frac{1}{1-\tau_a} a_h(v_h, v_h)$. If we restrict this to one Voronoi region and reorganize the terms we get

$$\frac{a(v_h, v_h)_{\mathcal{V}_k} - a_h(v_h, v_h)_{\mathcal{V}_k}}{a(v_h, v_h)_{\mathcal{V}_k}} \leq \tau_{k,a}. \quad (31)$$

If we further restrict ourselves to Voronoi regions where the bilinear form does not involve any boundary terms and make the estimate over all the Voronoi regions in one stencil as for the norm estimate (30), we have

$$\frac{\sum_{j \in \mathcal{I}_k} (\|\Delta v_h\|_{L_2(\mathcal{V}_j)}^2 - \|\Delta v_h\|_{\ell_2(\mathcal{V}_j)}^2)}{\sum_{j \in \mathcal{I}_k} \|\Delta v_h\|_{L_2(\mathcal{V}_j)}^2} = \frac{\sum_{j \in \mathcal{I}_k} v_h(X_j)^T (L^j - L^j) v_h(X_j)}{\sum_{j \in \mathcal{I}_k} v_h(X_j)^T L^j v_h(X_j)} \leq \tilde{\tau}_{k,a}. \quad (32)$$

As for the smoothing error, the matrix in the denominator has a polynomial nullspace, which is harmless, but needs to be removed when studying the eigenvalues, see Section 2.

For coercivity, we need the global constant to satisfy $\tau_a < 1$. Equality occurs when the discrete bilinear form is zero while the continuous bilinear form is non-zero. In the numerical experiments, we look for the smallest q_k for which this does not happen for any stencil in the test set.

5 Numerical experiments for the smoothing errors

To numerically calculate the bound in equation (24) we require two components. The first component is (continuous) norms of trial space functions and their derivatives over the overlapping regions and the second one is norms of weight functions and their derivatives over the same regions. The former are approximated by Monte Carlo integration on $N_H = 1500$ Halton nodes. To calculate the latter exactly, we would need to explicitly calculate the weight functions, which is beyond the scope of this paper. We instead consider one-dimensional problems along the lines between x_k and each interacting stencil center x_j for $j \in J_k$ and assume that the weight functions remain constant in the direction parallel with the shared edge of the central Voronoi region. This allows us to use one-dimensional integration over the direction normal to the edge, and then multiply the result by the length of the edge to obtain an approximation for the weight function integrals. The one-dimensional weight functions were computed using a C^1 B-spline as the generating function. This leads to a slight overestimate of the magnitude of the weight function where more than two patches overlap, but should not have a large effect on the overall bounds. Since the overlap at a corner in the outward edge direction is larger than the side overlap, also the derivatives should be slightly overestimated.

As is mentioned in Section 3, the smoothing error bounds are based on stencil-wise estimates and depend on the relative positions of the stencil nodes. It is therefore necessary to calculate the estimates on an ensemble of stencils to obtain a distribution of the possible values for the stencil-based estimates. The results presented in this section have been obtained from an ensemble of 500 stencils. The stencils are generated in the following way:

1. A set of $N_g = 10n$ background nodes are generated on the unit square. These are either random nodes drawn from a uniform distribution or Halton nodes selected as a subset of a longer sequence, where the starting point of the subset is randomized.
2. The most central node is selected as the stencil center.
3. The n nearest neighbours, including the center, are chosen as the stencil nodes.

It is often postulated in literature that the estimates of the type made in equation (18) depend on the node quality c_q . This was the first claim we wanted to put to the test. For each of the stencils generated on random nodes we calculated the node quality and plotted the smoothing error estimates against it. Such plots are given in Figure 4 for $\delta = 0.2$, $n = 2m$ and different values of p . We can see that there is no discernible relation between the node quality and the maximum eigenvalue when p is fixed. In our experiments, we did observe some dependence of the norm bound on the distance to the nearest node x_j with an overlapping \mathcal{V}_j^δ , but the dependence is not visible if the results are given in terms of node quality. However, as p is increased we can see a shift in the data towards lower node quality and towards higher values of the error estimates. These two effects are independent and the shift in the error estimates is the focus of this paper and is further investigated in the subsequent sections.

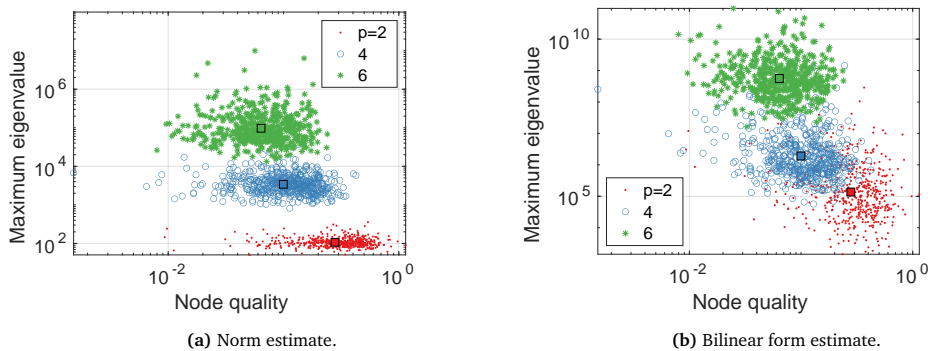


Figure 4: Plots of the maximum eigenvalues versus node quality for relative overlap parameter $\delta = 0.2$, and stencil size $n = 2m$. The square markers represent the geometric means of the respective point clouds.

The shift in node quality comes from two contributions related to the way the node quality is calculated for each generated stencil. The first contribution comes from the fact that we introduce the convex hull of the stencil nodes as the stencil boundary. When the ball which is used to determine the fill distance intersects the convex hull we need to reduce its diameter, which reduces the average fill distance. For polynomial degree $p = 2$ and $p = 4$, this happens in approximately half of the generated stencils. The second contribution comes from the fact that as more and more nodes are added to the stencil, the separation distance typically becomes smaller.

None of the contributions listed above introduce any significant dependence between the error estimates and the node quality and we can therefore assume that the node quality does not have a significant effect on these particular results, which means that we can focus on the behavior of the distribution of the error estimates without controlling for the node quality.

5.1 The norm bound

The distributions of the stencil estimates for the norm bound, over an ensemble of 500 stencils, are shown as box plots in Figure 5. The results are computed for relative overlap parameter values $\delta = 0.05, 0.2$ and 0.5 and polynomial degrees $p = 1, \dots, 6$. We produced results for three different stencil sizes for each polynomial degree p . A stencil size $n = 2m$, where m is the dimension of the polynomial basis, was recommended in [5] for approximations in two dimensions. We use this size, as well as a smaller size

$n = m + 1$ and a larger size $n = 3m$. We can see that in general, the bound increases as p and n are increased. By increasing these two parameters we get access to increasingly rich function spaces which allow us to construct functions that are more and more problematic for the kinds of estimates we are trying to make. For the same reason, the spread of the calculated estimates increases. As we increase the relative overlap δ , we notice that the trend breaks for large stencil sizes at $p = 5$ for $\delta = 0.2$ and $p = 4$ for $\delta = 0.5$. This happens because the matrix $M_{\mathcal{V}_k^{-\delta}}$ becomes numerically rank deficient and we have discarded the infinite eigenvalues of the generalized eigenproblem.

The second trend that we can observe is that on average the bound increases as δ is increased. This is expected, since we are trying to bound the norm of the function over the strip along the Voronoi region boundary in terms of the norm of the function in the interior of the region and the strip is getting wider as the overlap is increased. Another important observation that can be made about the data presented in Figure 5 is that there is no significant difference between Halton and random nodes. We can see that in general the boxes are slightly tighter for Halton nodes, but the extreme values have a similar order of magnitude.

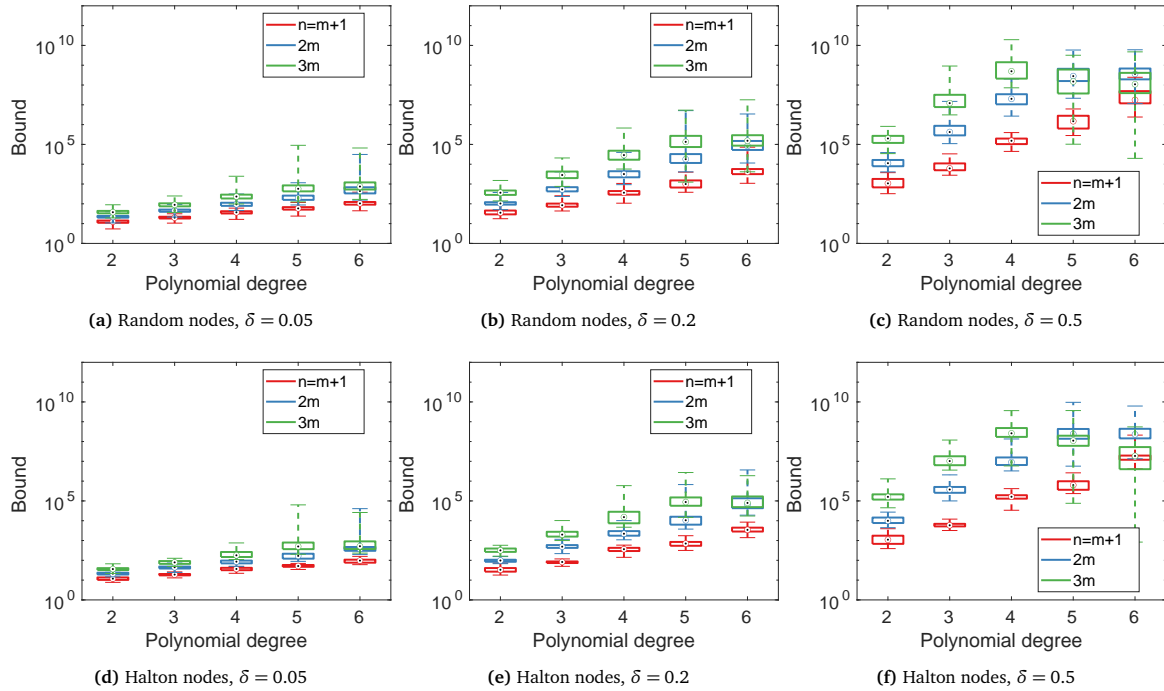


Figure 5: The distribution of stencil norm estimates for random nodes (top row) and for Halton nodes (bottom row). For each subplot, each stencil size n , and each polynomial degree p , a box plot illustrates the distribution of stencil estimates over 500 stencil realizations. The median stencil estimate is the center of the box, the box extends from the first to the third quartile of the results, and the extremal results are the endpoints of the lines with the same color as the box. Each box plot is produced by a separate set of 500 stencil realizations.

In Figure 6, we illustrate the type of function that corresponds to the worst case scenario for the norm bound. These are associated with the largest eigenvalue in the norm estimate. We evaluate and plot the function corresponding to the nodal values of the eigenvector over the stencil domain using (6). Functions are shown for several values of p and n , keeping $\delta = 0.5$. All of them are constructed from the same node arrangement. The central Voronoi region is labeled by a black polygon. We can see that the worst-case functions are almost zero on $\mathcal{V}_k^{-\delta}$ and increase rapidly over Γ_k^{δ} . Even though the function space gets enriched both by increasing p and m , we can see that the two parameters contribute differently to the worst-case functions. When increasing p we can see that the function gets flatter and closer to zero on $\mathcal{V}_k^{-\delta}$ and only rarely changes sign outside $\mathcal{V}_k^{-\delta}$. In contrast, increasing n allows the function to be closer to zero on $\mathcal{V}_k^{-\delta}$, but causes the function to change sign more often outside of $\mathcal{V}_k^{-\delta}$.

5.2 The bilinear form bound

The distributions of the calculated bilinear form stencil estimates are shown in Figure 7 for the same parameters and stencil realizations as the norm estimates. The eigenproblem associated with the bilinear form estimate (24) involves the Laplacian matrices $L_{\mathcal{V}_j}^j$ in the denominator and we have to use the strategy described in Section 2 to remove the polynomial null space. We observe as a general trend that the distribution of the estimates gets worse as the polynomial degree is increased, but in contrast with the norm bound, the estimates generally decrease as δ is increased. The reason for this behaviour is that the weight function derivative estimates decrease for a larger overlap parameter δ . The opposite behaviour of the bilinear form estimates and the norm estimates means that there is an optimal δ that minimizes the overall error estimate.

Comparing these plots with the norm bound plots in Figure 5 we also notice that the type of node arrangement used to construct the stencil significantly changes both the impact of n and the spread of the bilinear form bounds. For small p the increase in n improves the bounds in the case of random nodes but worsens the bound for Halton nodes. Importantly, the use of Halton nodes significantly reduces the range of the distribution of the estimates, regardless of n and p .

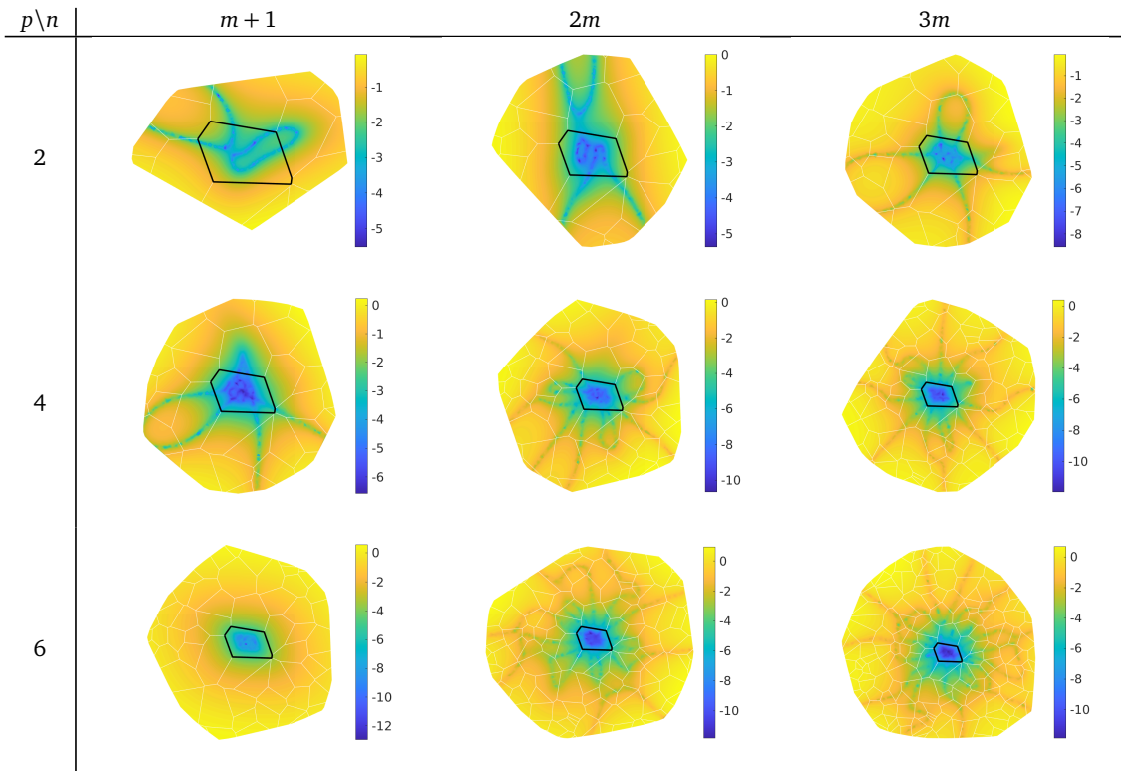


Figure 6: The functions $v_i(y)$ corresponding to the largest eigenvalue of the generalized eigenvalue problem in the norm estimate (22) for relative overlap parameter $\delta = 0.5$, polynomial degree $p = 2, 4, 6$, and stencil size $n = m + 1, 2m, 3m$. Note that we plot $\log_{10} |v_i|$ and that the range of the colour bar changes between subfigures.

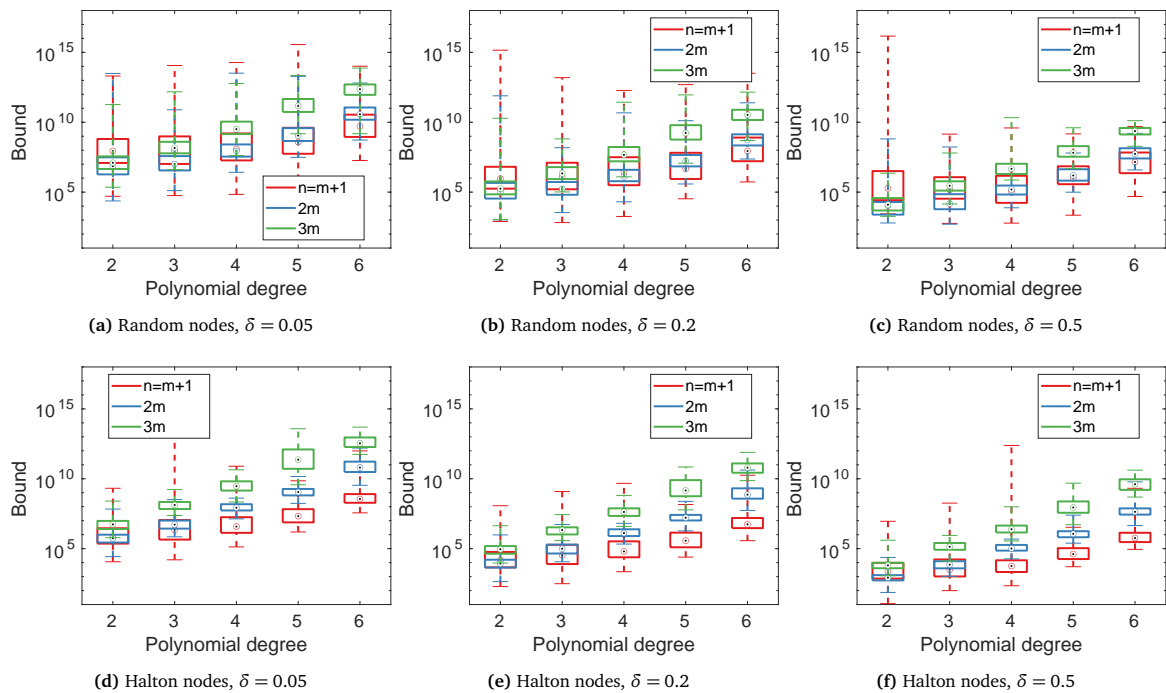


Figure 7: The distribution of stencil bilinear form estimates for random nodes (top row) and Halton nodes (bottom row). For each subplot, each stencil size n , and each polynomial degree p , a box plot illustrates the distribution of stencil estimates over 500 stencil realizations. The median stencil estimate is the center of the box, the box extends from the first to the third quartile of the results, and the extremal results are the endpoints of the lines with the same color as the box. Each symbol is produced by a separate set of 500 stencil realizations, while these are the same realizations as were used for the norm estimates shown in Figure 5.

In Figure 8 we illustrate the functions corresponding to the worst-case eigenvectors and in Figure 9 we illustrate their Laplacians. The definition of the generalized eigenvalue system in equation (24) combines the function values from several stencils, but we neglect the additional nodal values when generating the illustrations of the eigenvectors and only give the reconstruction on the central stencil. From the plots we can see that the function values illustrated in Figure 8 are dissimilar to the worst-case functions for the norm bound, but we notice similarities with the Laplacians illustrated in Figure 9 and the worst-case norm bound functions, with both types being flat and close to zero on $\mathcal{V}_k^{-\delta}$.

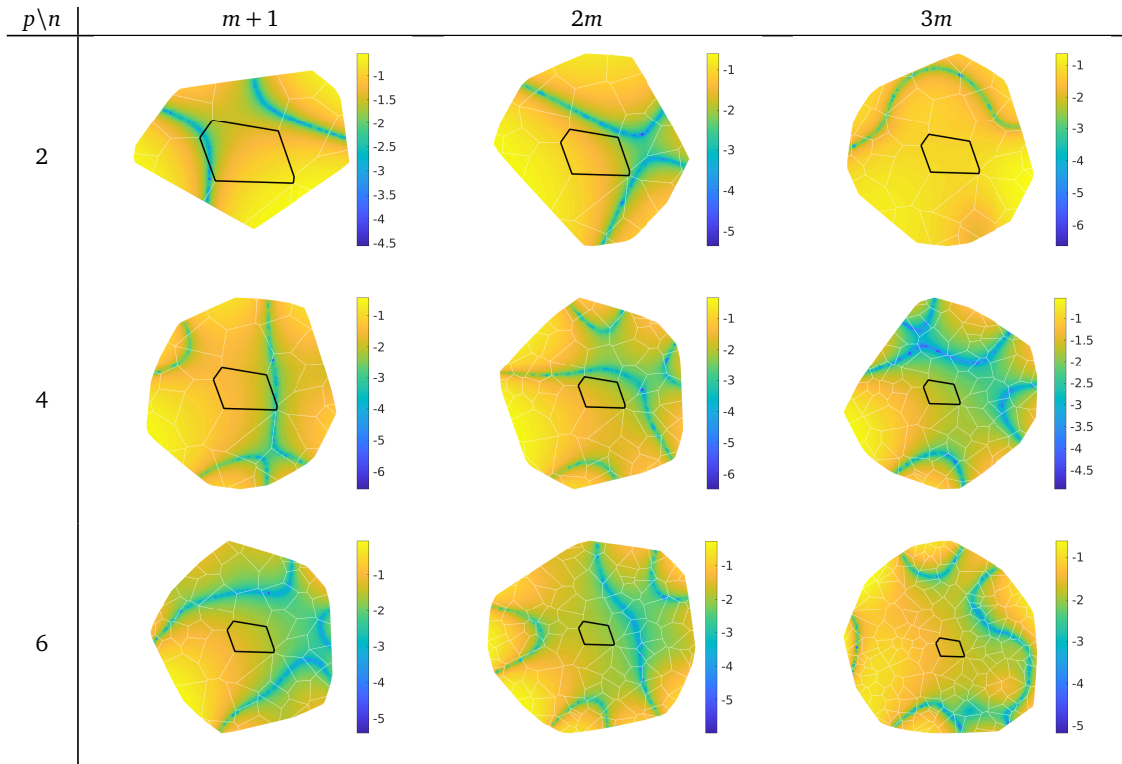


Figure 8: The functions $v_h(y)$ corresponding to the largest eigenvalue of the generalized eigenvalue problem in the bilinear form estimate (24) for relative overlap parameter $\delta = 0.5$, polynomial degree $p = 2, 4, 6$, and stencil size $n = m + 1, 2m, 3m$. Note that we plot $\log_{10}|v_h|$ and that the range of the colour bar changes between subfigures.

5.3 Smoothing experiments for a one-dimensional problem

As mentioned in Section 3, we believe that the smoothing error estimates are quite pessimistic both due to the use of a local worst case over every stencil, and due to the upper bound on the partition of unity sum, including the norms of the differentiated weight functions.

To further investigate this, we turn to a one-dimensional problem, where we can compute both local and global worst case eigenfunctions directly with actual weight functions. We use the Wendland function [12] $\varphi_{3,1}(r) = (1-r)_+^4(4r+1)$, which is C^2 and positive definite in one, two and three space dimensions, as generating function for the weights. We approximate the generalized eigenvalue problems for the norms $\|v_h\|_{L_2(\cdot)}^2 / \|v\|_{L_2(\cdot)}^2$ (not for the bound) both locally in one Voronoi region and globally over Ω . Figures 10a and 10b show the local and global functions with the largest eigenvalues. Locally, we get $\eta_{0,k} \lesssim 70$, while globally $\eta_0 \approx 0.002$, which confirms that using a local bound affects the global estimate negatively.

The smoothing error depends on the size of the jumps at the Voronoi edges. As discussed in [10], the errors in the local approximations, and consequently the jumps between Voronoi regions, depend on the $p+1$ -order derivative of the function that the data is generated from. This tells us that oscillatory data, creating high derivatives at each Voronoi interface, should be particularly challenging. This can also be understood from the perspective that such a function is not very well resolved by the discretization. As can be seen in Figure 10b, the worst function for the overall smoothing error is oscillatory, but the error is still small.

For the norm of the Laplacian, we have only computed the global worst case function, shown in Figures 10c and 10d. Again, the worst case result is an oscillatory function. The smoothing error $\eta_a \approx 0.3$ is larger than for the norm, but significantly smaller than the computed bounds from the previous subsection. The results for this problem suggest that the smoothing error is likely to be harmless also in higher dimensions as long as the node points are well distributed.

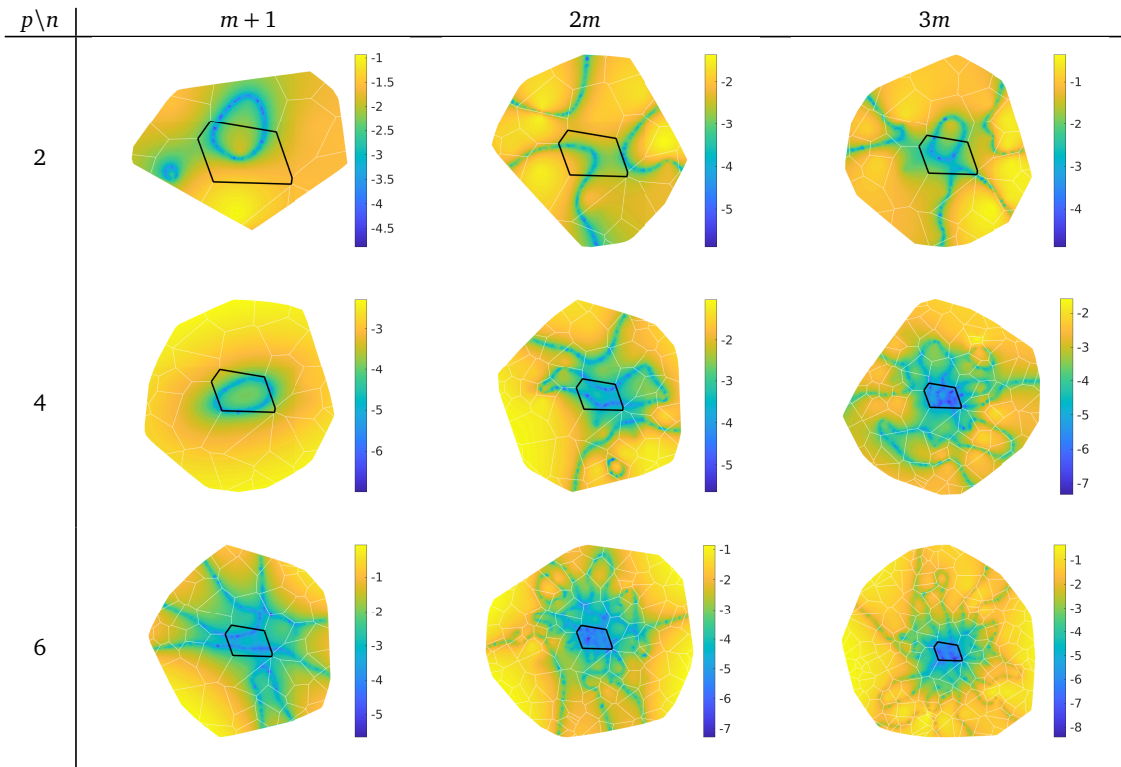


Figure 9: The Laplacian of the functions $v_h(y)$ corresponding to the largest eigenvalue of the generalized eigenvalue problem in the bilinear form estimate (24) for relative overlap parameter $\delta = 0.5$, polynomial degree $p = 2, 4, 6$, and stencil size $n = m + 1, 2m, 3m$. Note that we plot $\log_{10} |\Delta v_h|$ and that the range of the colour bar changes between subfigures.

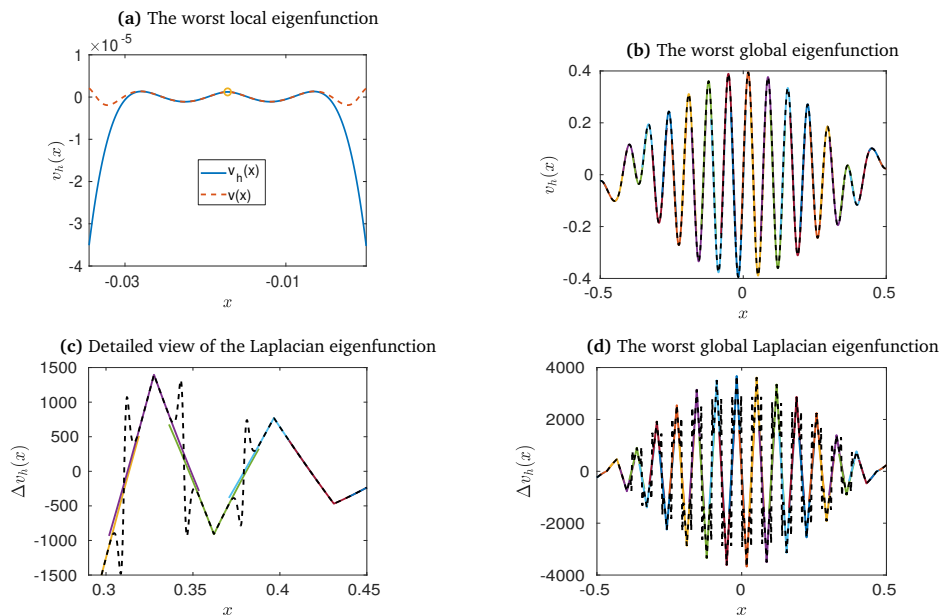


Figure 10: The worst local and global eigenfunctions for the norm (top row) and the worst global eigenvector for the norm of the Laplacian (bottom row) with overlap parameter $\delta = 0.5$ polynomial degree $p = 4$, stencil size $n = 7$, over $N = 30$ uniform nodes. In each subfigure the local stencil approximation(s) v_h^k over the extended Voronoi region(s) (solid line) and the smoothed trial space function v (dashed line) are shown. For the illustrated worst case functions the true smoothing errors are (a) $\eta_{0,k} \approx 70$ for the norm over one Voronoi region (b) $\eta_0 \approx 0.002$ for the norm globally (c)–(d) $\eta_a \approx 0.3$ for the norm of the Laplacian globally.

6 Numerical experiments for the integration errors

For our numerical experiments we compute the largest eigenvalue $\tilde{\tau}_{k,0}$ given by the generalized eigenproblem in equation (30) and the largest eigenvalue $\tilde{\tau}_{k,a}$ given by equation (32). The overall integration error estimate for one stencil is then given by $(1 + \tilde{\tau}_{k,0})/(1 - \tilde{\tau}_{k,a})$. Both the norm and bilinear form bounds are computed over the domain $\mathcal{D} = \cup_{j \in \mathcal{I}_k} \mathcal{V}_j$, where \mathcal{I}_k contains the indices of the nodes in stencil k . The local mass and stiffness matrices, M_h^i, L_h^j are computed for each contributing stencil and are assembled to construct the global matrices $\mathcal{M}_h, \mathcal{L}_h$, where $\|v_h\|_{\ell_2(\mathcal{D})}^2 = v_h^T(X_{\mathcal{D}})\mathcal{M}_h v(X_{\mathcal{D}})$, $a_h(v_h, v_h)_{\mathcal{D}} = v_h^T(X_{\mathcal{D}})\mathcal{L}_h v(X_{\mathcal{D}})$, $X_{\mathcal{D}}$ is the combined node set, and $|X_{\mathcal{D}}| \equiv N_e \approx 3n$ is the size of the extended system used for the integration. The continuous norm global matrices are similarly estimated using a large number, $N_H = 10^4$, of Halton nodes over each of the involved Voronoi regions.

An equal number of quadrature points, $q_k = q$ is used for all Voronoi regions. As explained in Section 4, the bounds break down if $\tilde{\tau}_{k,0} = -1$ or $\tilde{\tau}_{k,a} = -1$ which occurs if $\text{rank}(\mathcal{M}_h) < N_e$ or $\text{rank}(\mathcal{L}_h) < \text{rank}(\mathcal{L})$. Specifically, we expect the mass matrix \mathcal{M}_h to have full rank and we expect \mathcal{L}_h and \mathcal{L} to have the same nullspace.

The extended system size is dependent on the positions of the stencil nodes. Hence, just as in the smoothing error estimates we compute results for an ensemble of stencils. The distribution of extended system sizes, N_e , is shown in Figure 11. The box plots are constructed using data from 100 realizations.

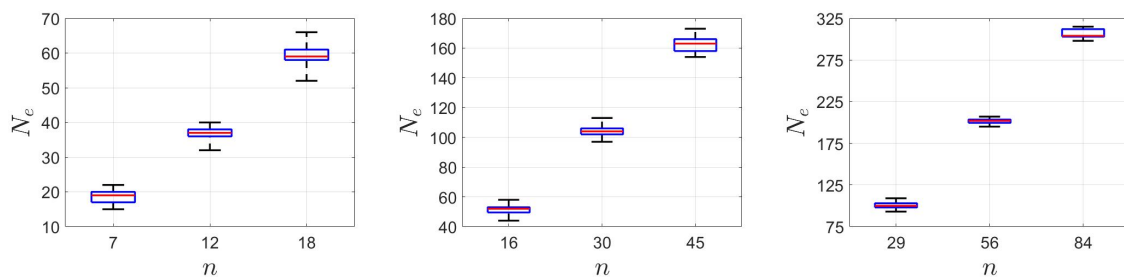


Figure 11: Box plots of the extended problem size N_e used in the integration over stencil \mathcal{D} for different stencil sizes $n = m + 1, 2m, 3m$. The results were obtained from 100 realizations of stencils constructed using Halton nodes.

Additionally, we provide the numerically estimated minimal oversampling values for which the bounds do not break down. Table 1 gives the minimum number of local quadrature points q for which, following 100 realizations, the global discrete mass and stiffness matrices, $\mathcal{M}_h, \mathcal{L}_h$, have equal rank to their continuous counterparts, \mathcal{M}, \mathcal{L} . We provide the actual oversampling used, based on the global definition of oversampling applied to the central stencil, $\frac{|Y|}{|X|} = \frac{qn}{N_e}$. The results suggest that the minimum oversampling is independent of the polynomial degree p and the stencil size n .

	$n = m + 1$		$n = 2m$		$n = 3m$	
	q_{\min}	$q_{\min}n/N_e$	q_{\min}	$q_{\min}n/N_e$	q_{\min}	$q_{\min}n/N_e$
$p = 2$	7	2.57	5	1.62	8	2.44
$p = 3$	6	2.00	7	2.09	6	1.73
$p = 4$	7	2.15	6	1.73	7	1.93
$p = 5$	8	2.35	7	1.95	8	2.20
$p = 6$	6	1.74	7	1.94	6	1.66

Table 1: The smallest number of local quadrature points q_{\min} and oversampling factor $q_{\min}n/N_e$ for which the method is stable for polynomial degree p and stencil size n . The median value of the extended system size N_e , see Figure 11, was used to calculate the oversampling.

The distributions of the local integration error bounds for polynomial orders $p = 2, p = 4, p = 6$ are provided in Figures 12, 13, 14, respectively. The bounds $\tilde{\tau}_{k,0}$ and $\tilde{\tau}_{k,a}$ are computed for 100 different stencils and plotted against the local number of quadrature points q , starting from $q = 6$ for each polynomial order, p and stencil size, n . We expect from the global integration error estimate in equation (28), and the Monte Carlo integration bound in [10] that the bounds will decrease as the oversampling is increased. This is also the case for the overall bound shown in the rightmost subfigures. It is less clear for the norm bound with smaller stencil sizes, while the bilinear form also displays a decreasing trend.

It should be noted that what we see here is not the convergence of a quadrature rule for a given function. Instead, we observe the worst overestimate of the norm for any function in the trial space and the worst underestimate of the bilinear form for any function in the trial space. Since the quadrature points move, the worst function also changes with the point locations. The results are consistently worse with larger m and larger p as for the smoothing error. This is expected since the function space containing the functions over which we integrate is enlarged in both cases.

We also performed experiments for stencils generated from random nodes, but it is clear that it is hard or impossible to guarantee stability, since the node quality can be arbitrarily bad. We made a slightly different definition of q_{\min} and tried to locate the smallest q such that no stencil is rank deficient for any $q \in [q_{\min}, q_{\min} + 4]$, indicating a low probability of failure. Table 2 shows results for three polynomial degrees. For degree $p = 6$ we did not find a stable value for q_{\min} for all stencil sizes, while for

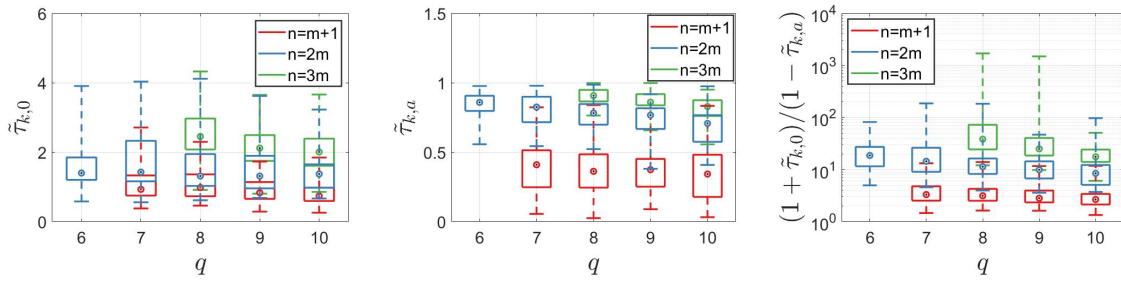


Figure 12: Box plots of integration error bounds against the number of local quadrature points q for polynomial degree $p = 2$. The results were obtained from 100 stencils constructed using Halton nodes. From left to right: norm bound $\tilde{\tau}_{k,0}$, bilinear form bound $\tilde{\tau}_{k,a}$, integration bound $(1 + \tilde{\tau}_{k,0}) / (1 - \tilde{\tau}_{k,a})$.

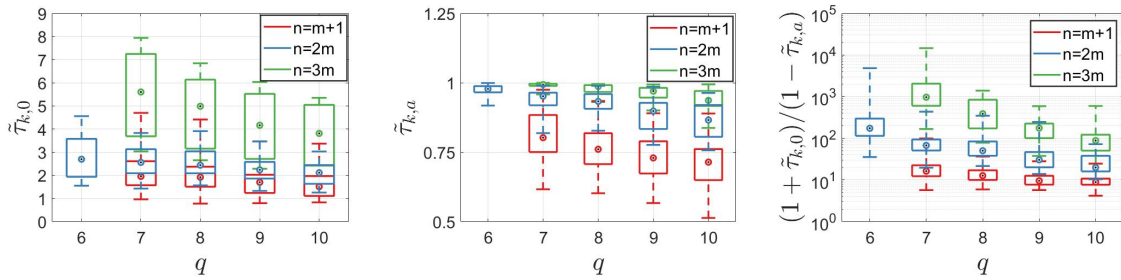


Figure 13: Box plots of integration error bounds against the number of local quadrature points q for polynomial degree $p = 4$. The results were obtained from 100 stencils constructed using Halton nodes. From left to right: norm bound $\tilde{\tau}_{k,0}$, bilinear form bound $\tilde{\tau}_{k,a}$, integration bound $(1 + \tilde{\tau}_{k,0}) / (1 - \tilde{\tau}_{k,a})$.

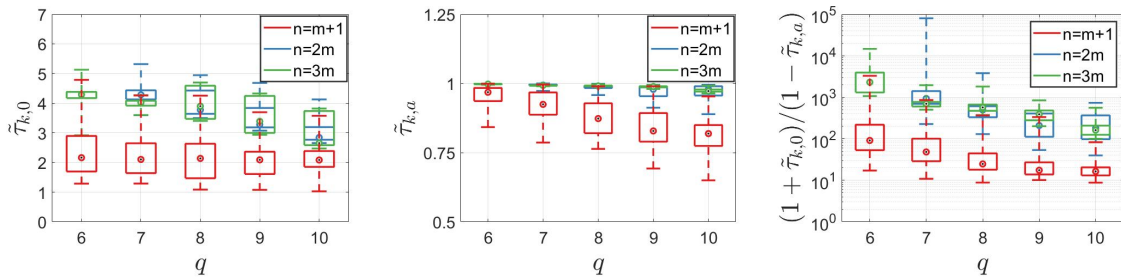


Figure 14: Box plots of integration error bounds against the number of local quadrature points q for polynomial degree $p = 6$. The results were obtained from 100 stencils constructed using Halton nodes. From left to right: norm bound $\tilde{\tau}_{k,0}$, bilinear form bound $\tilde{\tau}_{k,a}$, integration bound $(1 + \tilde{\tau}_{k,0}) / (1 - \tilde{\tau}_{k,a})$.

$p = 2$ and $p = 4$ it was possible at an oversampling factor between 3 and 6, which is around double that needed for stencils based on Halton nodes. Noteworthy, however, is perhaps that it was easier to find a stable result for $n = 2m$, the recommended stencil size, than for both the smaller and larger stencil size. Figure 15 shows the distributions of the local integration error bounds for 100 stencils constructed using random nodes. We note that the relation of the bounds to the number of local quadrature points q , and stencil size n is similar to the bounds computed using Halton nodes, however, at a significantly larger oversampling factor.

We go back to the results when the stencils are generated using Halton nodes, and in Figures 16 and 17, show plots of the eigenvector corresponding to the largest eigenvalue from the generalized eigenproblems in equations (30) and (32), respectively. The function is plotted over \mathcal{D} and is evaluated on each contributing Voronoi region using the corresponding stencil. The central Voronoi region is marked by black edges and the colour bar indicates the common logarithm of the function value. We note that the function values in Figure 16 are very small in most of the domain. Each of these functions also have a small region adjacent to the outer edge of the domain where it attains its maximum. The functions in Figure 17, for the bilinear form, are less localized, but also show a preference for being larger towards an outer edge. Figure 18 shows the Laplacian of the same functions. This shows the same behaviour as the worst functions for the norm, with a localized maximum at the outer edge. The Laplacian for $p = 2$ and $n = m + 1$ looks a bit odd, but this is because the Laplacian of the polynomial part of the approximation is constant and the PHS basis functions only have one degree of freedom due to the m constraints, see equation (2).

To go a bit deeper into why these functions are the worst for integration, Figure 19 shows the worst cases for one particular stencil both in linear and logarithmic scale. The worst function for the norm bound (left column) attains its maximum at the southeast corner of the integration domain. One of the quadrature points is placed right at the maximum, which leads to an

	$n = m + 1$		$n = 2m$		$n = 3m$	
	q_{\min}	$q_{\min}n/N_e$	q_{\min}	$q_{\min}n/N_e$	q_{\min}	$q_{\min}n/N_e$
$p = 2$	7	2.88	10	3.53	12	3.79
$p = 4$	15	5.76	14	4.12	18	5.00
$p = 6$	>84	>24.4	54	14.9	>100	>27.0

Table 2: The smallest number of local quadrature points q_{\min} and oversampling factor $q_{\min}n/N_e$ for which the method is stable for polynomial degree p and stencil size n when the stencils are based on random nodes. The median value of the extended system size N_e , was used to calculate the oversampling. For the values with $>$, no stable q_{\min} was found within the search range.

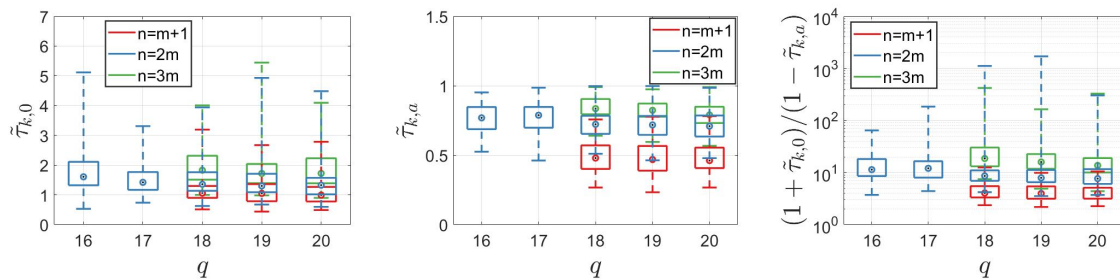


Figure 15: Box plots of integration error bounds against the number of local quadrature points q for polynomial degree $p = 4$. The results were obtained from 100 stencils constructed using random nodes. From left to right: norm bound $\tilde{\tau}_{k,0}$, bilinear form bound $\tilde{\tau}_{k,a}$, integration bound $(1 + \tilde{\tau}_{k,0}) / (1 - \tilde{\tau}_{k,a})$.

overestimate of the continuous integral. The Laplacian of the worst function for the bilinear form bound (right column) attains its maximum in the Voronoi region just to the right of the one where the other function had its maximum. In this case, the quadrature points have a gap right there, such that the large values go undetected, leading to a gross underestimate of the integral. The discrete quadrature in this case only yields 3% of the value of the continuous bilinear form. Both types of estimates will improve as q is increased as the local maximum has to have a certain width, relating to p and n , and as we fill up the space, it will be sampled more frequently. However, the node quality plays an important role here. A small separation distance leads to high gradients in the cardinal functions, and in turn allows for functions that can be more localized. This is one argument for why random node stencils require a much higher oversampling to ensure stability.

7 Discussion

When we started writing this paper, we thought that node quality would be very important for stability of the RBF-FD method. It is the most important factor, but not in exactly the way we expected. For the smoothing errors, the node quality has no visible effect on the norm bound. For the bilinear form bound, the eigenvalues of the terms based on the RBF-FD matrices are not affected, while the weight function bounds depend on how close neighbouring nodes are to each other. For the integration error, the amount of oversampling that is needed for stability is significantly larger for the low node quality stencils generated over random nodes compared with the high node quality stencils generated over quasi uniform Halton nodes. Since random nodes can have arbitrarily small separation distance, we may need a very high oversampling rendering the method so computationally expensive that it cannot be practically used. That is, we need to ensure a reasonable node quality for example through using quasi uniform nodes. That node quality is important is of course already well known, but we think that our experiments add some understanding to how it interacts with stability.

We also note that at least in our experimental setup for the integration error, which can be seen as an unfitted RBF-FD approximation, where some nodes are outside the domain [9], it would be beneficial to have more evaluation points in the Voronoi regions close to the boundary to compensate for the lack of information outside of the domain. In this way, it would be possible to decrease the overall oversampling factor.

The smoothing bounds give rather large results and are the main contributors to the numerical stability constant in (18), assuming the node quality is bounded from below. Looking at which functions make these bounds large, we can draw a few conclusions. The functions that make the smoothing bounds large are different from the ones that make the integration errors large. The worst functions for the integration error are close to zero, or have a Laplacian that is close to zero, almost everywhere and have an small region with larger values. For the smoothing bound, it is bad if the function or its Laplacian is almost zero in the central Voronoi region, and then growing quickly towards the edges of the stencil. This cannot happen in all stencils at the same time, which means that the actual overall result should be better than the smoothing bound. In fact, the discussion and experiments for a one-dimensional problem in Section 5.3 indicate that the functions that give the worst smoothing errors are highly oscillatory, and that the global smoothing errors are not that large for well-distributed nodes.

We have also investigated the influence of the polynomial degree and the stencil size. A higher polynomial degree makes all bounds larger, such that there is a trade-off between error constant and convergence rate. We get a similar result for larger stencil sizes, but we believe that this might change somewhat if the overlap between stencils was taken into account in the smoothing error bounds. That is, it may be a result of our method of investigation rather than a real effect. As was shown in [9] the jumps

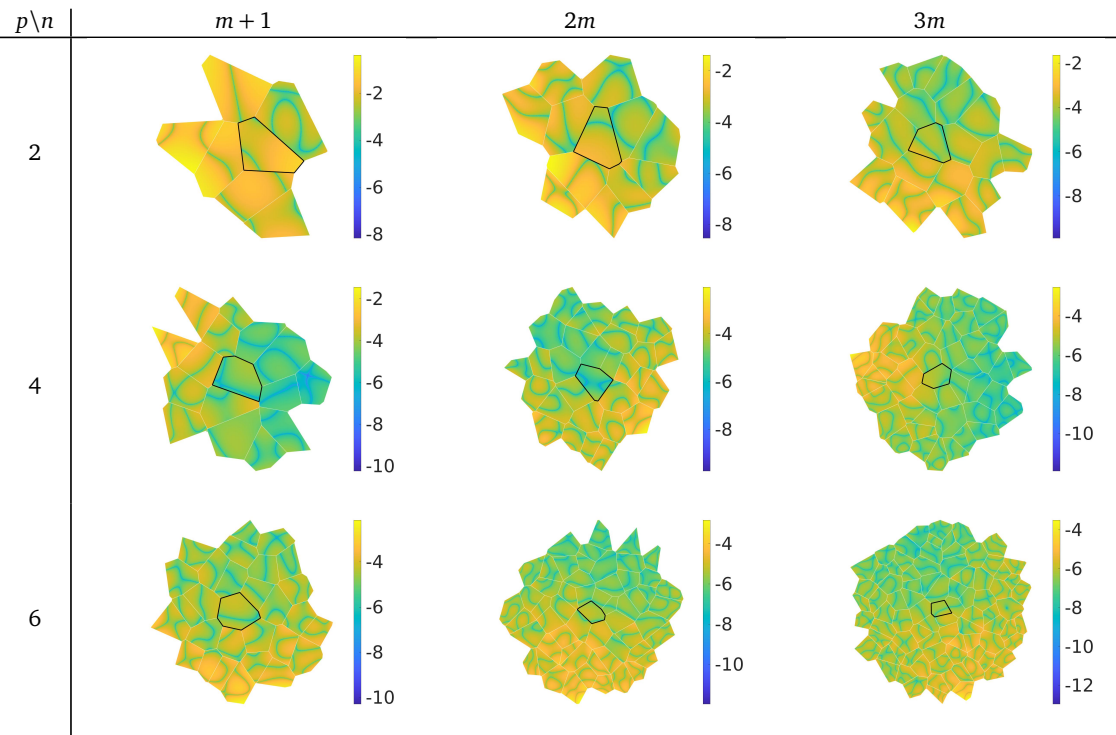


Figure 16: The functions $v_h(y)$ corresponding to the largest eigenvalue of the generalized eigenvalue problem in the norm integration error estimate for $q = q_{\min}$ given in Table 1. The functions are evaluated using the central Voronoi region stencil and plotted over the whole stencil. Note that we plot $\log_{10} |v_h|$ and that the range of the colour bar changes between subfigures.

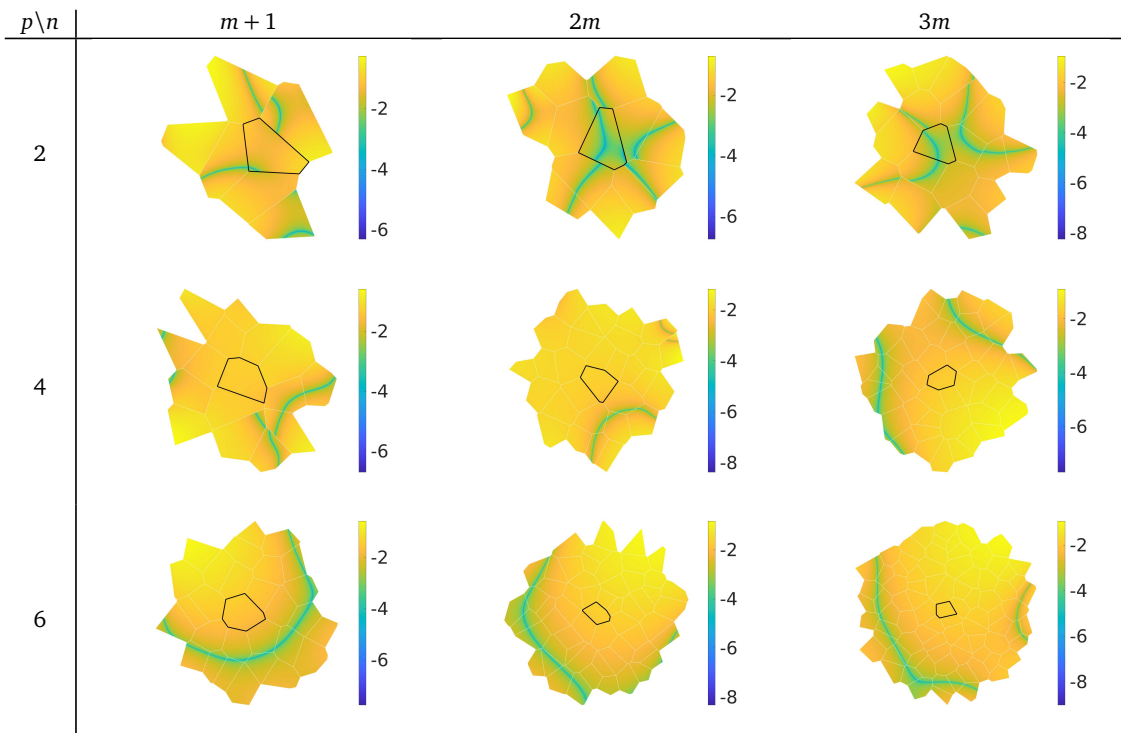


Figure 17: The functions $v_h(y)$ corresponding to the largest eigenvalue of the generalized eigenvalue problem in the bilinear form integration error estimate for $q = q_{\min}$ given in Table 1. The functions are evaluated using the central Voronoi region stencil and plotted over the whole stencil. Note that we plot $\log_{10} |v_h|$ and that the range of the colour bar changes between subfigures.

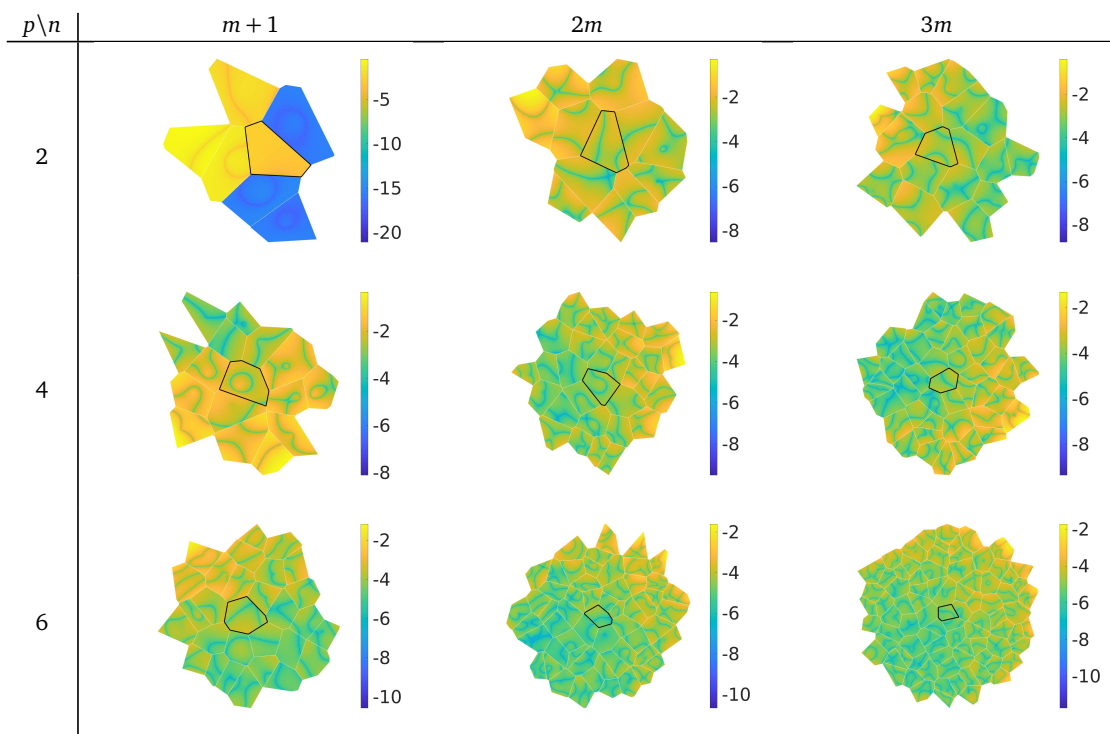


Figure 18: The Laplacian of the functions $v_h(y)$ corresponding to the largest eigenvalue of the generalized eigenvalue problem in the bilinear form integration error estimate for $q = q_{\min}$ given in Table 1. The functions are evaluated using the central Voronoi region stencil and plotted over the whole stencil. Note that we plot $\log_{10} |\Delta v_h|$ and that the range of the colour bar changes between subfigures.

in the cardinal functions, which are the reason we need a smoothing error estimate, decrease with stencil size.

Acknowledgements

The first and the third authors were supported by the Swedish Research Council under grant number 2020-03488. The second author was supported by the Swedish strategic initiative eSSSENCE and partially by the Slovenian research agency ARRS through program group P2-0162. The fourth author was supported by the Iran Ministry of Science and Technology. The computations were enabled by resources in project SNIC 2021/22-457 provided by the Swedish National Infrastructure for Computing (SNIC) at UPPMAX, partially funded by the Swedish Research Council through grant agreement no. 2018-05973.

References

- [1] D. Anisimov, D. Panozzo, and K. Hormann. Blended barycentric coordinates. *Comput. Aided Geom. Des.*, 52–53:205–216, 2017.
- [2] V. Bayona. An insight into RBF-FD approximations augmented with polynomials. *Comput. Math. Appl.*, 77:2337–2353, 2019.
- [3] V. Bayona, N. Flyer, and B. Fornberg. On the role of polynomials in RBF-FD approximations: III. Behavior near domain boundaries. *J. Comput. Phys.*, 380:378–399, 2019.
- [4] V. Bayona, N. Flyer, B. Fornberg, and G. A. Barnett. On the role of polynomials in RBF-FD approximations: II. Numerical solution of elliptic PDEs. *J. Comput. Phys.*, 332:257–273, 2017.
- [5] N. Flyer, B. Fornberg, V. Bayona, and G. A. Barnett. On the role of polynomials in RBF-FD approximations: I. Interpolation and accuracy. *J. Comput. Phys.*, 321:21–38, 2016.
- [6] B. Fornberg and N. Flyer. *A primer on radial basis functions with applications to the geosciences*, volume 87 of *CBMS-NSF Regional Conference Series in Applied Mathematics*. Society for Industrial and Applied Mathematics (SIAM), Philadelphia, PA, 2015.
- [7] V. Shankar, A. Narayan, and R. M. Kirby. RBF-LOI: augmenting radial basis functions (RBFs) with least orthogonal interpolation (LOI) for solving PDEs on surfaces. *J. Comput. Phys.*, 373:722–735, 2018.
- [8] D. Shepard. A two-dimensional interpolation function for irregularly-spaced data. In *Proceedings of the 1968 23rd ACM National Conference*, ACM ’68, pages 517–524, New York, NY, USA, 1968. ACM.
- [9] I. Tominec and E. Breznik. An unfitted RBF-FD method in a least-squares setting for elliptic PDEs on complex geometries. *J. Comput. Phys.*, 436:Paper No. 110283, 24, 2021.
- [10] I. Tominec, E. Larsson, and A. Heryudono. A least squares radial basis function finite difference method with improved stability properties. *SIAM J. Sci. Comp.*, 43:A1441–A1471, 2021.
- [11] I. Tominec, M. Nazarov, and E. Larsson. Stability estimates for radial basis function methods applied to time-dependent hyperbolic PDEs, 2021.

[12] H. Wendland. Piecewise polynomial, positive definite and compactly supported radial functions of minimal degree. *Adv. Comput. Math.*, 4(4):389–396, 1995.

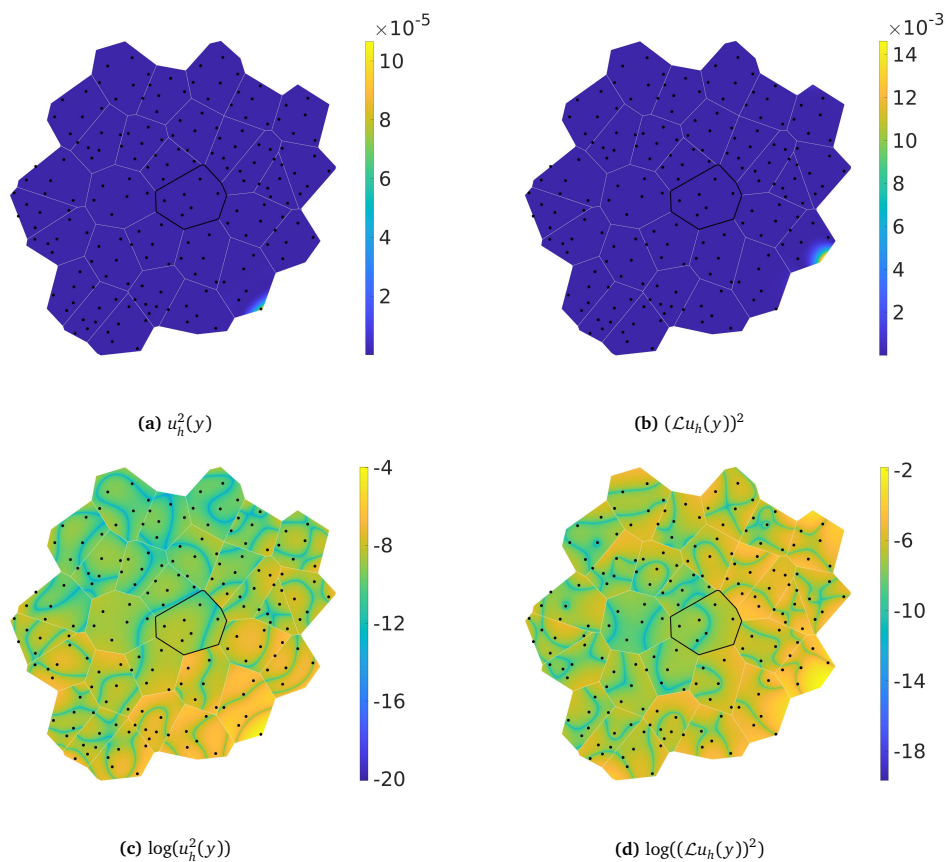


Figure 19: The squared function corresponding to the maximum eigenvalue $\tilde{\tau}_{k,0} = 4.35$ from the norm bound (left column) and the squared Laplacian of the function corresponding to the maximum eigenvalue $\tilde{\tau}_{k,\alpha} = 0.97$ from the bilinear form bound (right column) plotted together with the qn quadrature points $Y_{\mathcal{D}}$ in linear scale (top row) and logarithmic scale (bottom row).